PNAS RESEARCH ARTICLE | APPLIED PHYSICAL SCIENCES

# Vapor-mediated wetting and imbibition control on micropatterned surfaces

Ze Xu[a,1], Raphael Saiseau[a], Olinka Ramírez Soto[a,b], and Stefan Karpitschka[a,1]

Affiliations are included on p. 6.

Edited by Howard Stone, Princeton University, Princeton, NJ; received July 22, 2025; accepted December 1, 2025

**Wetting of micropatterned surfaces is ubiquitous in nature and key to many technological applications like spray cooling, inkjet printing, and semiconductor processing. Overcoming the intrinsic, chemistry- and topography-governed wetting behaviors often requires specific materials which limits applicability. Here, we demonstrate that droplet spreading and wicking on hydrophilic patterns can be controlled by the vapor of a lower-surface-tension liquid. Condensation of the vapor induces Marangoni forces that delay capillary wicking and contract liquid into a droplet on top of the imbibed film. Thereby, macroscopic droplets can be maintained in an apparent partial wetting state, effectively cloaking the pattern. We quantify how pattern characteristics and vapor condensation compete, balancing in different wetting states from pinning to complete imbibition. Since this balance is the result of nonequilibrium processes rather than static wetting phenomena, it can be reversibly tuned by modifying the vapor concentration. This way, we guide droplets across patterns and even extract previously imbibed liquids, devising strategies for coating, cleaning, and drying functional surfaces.**

droplet evaporation | Marangoni stress | imbibition | surface processing | droplet manipulation

Controlling the wetting behavior of droplets on surfaces is crucial to many industrial fields, such as semiconductor surface processing, inkjet printing, or coating technology (1). The morphology of sessile droplets is primarily governed by surface chemistry and topography, liquid composition, and external stimuli including atmospheric composition as well as electric or magnetic fields (2, 3). Overcoming system-intrinsic wetting behaviors to, e.g., apply defect-free coatings (4) or dry fragile structures nondestructively (5) remains a ubiquitous challenge, largely because choices of surface chemistry, topography, or tolerance to electric fields are usually constrained by the final application.

Rationally designed surface topographies, often inspired by pillar or groove structures found in nature, enable unique wetting properties ranging from superhydrophilicity to superhydrophobicity (6). The intermediate regime of hemiwicking (7), where sessile droplets emit wicking films into the structures, is particularly interesting for surface processing. Evolution and geometry of the wicking film are governed by pillar shape and pattern (8–10), allowing the design of dedicated functions like deposit shaping (10), unidirectional spreading (11–13), or liquid diodes (14). A high liquid volatility may alter and temporarily suppress the evolution of the wicking film (15). A complementary approach for droplet control is the spatial modulation of the liquid composition, e.g., by selective evaporation/condensation of binary (16, 17) or ternary (18) mixtures, leading to so-called Marangoni contraction (17) or spreading (19): Gradual depletion and enrichment of different chemical species toward the edge of a droplet induce surface tension gradients that drive Marangoni flows, leading to a wetting or dewetting motion, or altering the apparent contact angle (16–20). Counteracting topography-induced hemiwicking with vapor-mediated Marangoni forces could leverage dynamic control over wetting and imbibition on textured surfaces. Crucially, this approach could also tolerate constraints on topography and/or material choice imposed by the final application. Yet, this combination remains unexplored in scientific literature.

Here, we demonstrate that the spreading and imbibition dynamics of sessile droplets of various binary mixtures on hemiwicking surface topographies are upended by selective condensation/evaporation in a nonequilibrium vapor environment, although both liquids individually wet and wick the patterns. The surface structures enhance wettability because the equilibrium (microscopic) contact angle is below a critical value governed by the roughness parameters of the texture, thus generating a capillary wicking force (7). Without compositional gradients, the resulting dynamics are akin to

## Significance

Topographic patterning of surfaces is central to microfabrication technologies. The capillary action of the patterns can be a significant challenge for fabrication and application, especially as length scales are minimized. Here, we demonstrate that the vapor of a lower surface tension liquid, miscible with the wetting fluid, upends wetting and imbibition on textured surfaces. We show that imbibition can be delayed, inhibited, and even reverted, depending on a balance between Marangoni and capillary forces that can be tuned dynamically through the vapor composition. These fundamental insights on nonequilibrium wetting phenomena enable tailored processing strategies for microelectronics, mechanical microstructures, or printing technology, where application-governed design often conflicts with wetting requirements.

Author contributions: S.K. conceived the study; Z.X., O.R.-S., and S.K. designed research; Z.X. performed research; Z.X. and R.S. analyzed data; R.S. developed the model; Z.X., R.S., and S.K. wrote the first draft of the paper; and all authors contributed to the interpretation of the data, discussions of the results and writing of the manuscript.

The authors declare no competing interest.

This article is a PNAS Direct Submission.



[1]To whom correspondence may be addressed. Email: ze.xu@uni-konstanz.de or stefan.karpitschka@uni-konstanz.de.

This article contains supporting information online at https://www.pnas.org/lookup/suppl/doi:10.1073/pnas.2519761122/-/DCSupplemental.

Published January 2, 2026.

the Washburn law, describing the liquid front wicking into a porous material (21, 22), potentially modified by evaporation for highly volatile liquids (15). Imposing excess vapor of the lower surface tension component, however, we observe an extreme delay or, initially, even complete inhibition of the wicking, leading to a prolonged coexistence of a macroscopic droplet body surrounded by an imbibition film of finite extent (Fig. 1 and Movie S1). Remarkably, the droplet remains free to move as the film cloaks the surface topography. We demonstrate that this is an out-of-equilibrium phenomenon driven by surface tension gradients rather than static surface energies. Absorption of excess vapor causes Marangoni flows which compensate for the capillary action of the micropattern, normally responsible for spreading and wicking. Exploiting this antagonism, we explore strategies for droplet manipulation and even extraction of imbibed liquids. We show that this effect can be implemented with a wide range of surface topographies and liquid parameters, thus retaining a significant degree of freedom in design choices, giving it a promising potential for technological applications.

## 1. Results

**1.1. Experimental Approach.** Experiments were performed on canonical surface topographies, i.e., micropillar arrays fabricated by direct laser writing (resolution ∼300 nm) of an SU-8 photoresist on silicon wafers (Fig. 1*A*). Unless stated otherwise, pillars were cube-shaped with 10 µm edge length, arranged on a square lattice with varying spacing $S$, and hydrophilized by plasma treatment before use. Experiments with various pillar aspect ratios and sizes are shown in *SI Appendix*, Extended Data Figs. S1–S3. We used water, ethylene glycol (EG), and binary mixtures of water and isopropyl alcohol (IPA) as test substances for droplets, and the vapors of ethanol, water, and IPA for the gas phase (*SI Appendix*, Extended Data Fig. S4). All liquids immediately wick fully into these patterns in dry atmosphere or vapor of the same liquid (pure cases; see *SI Appendix*, Extended Data Fig. S5 and Movie S7). Experiments were performed in an environmental chamber (Fig. 1*A*) at constant room temperature (∼21 °C), constantly feeding nitrogen gas with the desired vapor content to two inlet chambers which, across membranes, diffusively exchange gases with the main chamber (Fig. 1*A*). Vapor compositions were varied by bubbling nitrogen through gas wash bottles containing pure liquids or binary mixtures of mass fraction $\tilde{c}$. The wetting and wicking dynamics were imaged from top and side through windows. Further details are provided in *Materials and Methods*.

**1.2. Delayed Wicking.** Depositing a droplet of pure water at time $t = 0$ onto a surface with pillar spacing $S = 30$ µm in an IPA-vapor environment (Fig. 1*B* and Movie S1), the droplet does not readily spread across or wick into the surface pattern, as was observed in dry or humid ambient (*SI Appendix*, Extended Data Fig. S5). Rather, the droplet remains in a spherical-cap-like shape, while a wicking film slowly emerges from its periphery (≳100 times slower than in the pure case). Long-distance video microscopy from the top and the side reveals the local topography of the liquid surface (Fig. 1*C*), which is sketched in Fig. 1*D*: The droplet surface merges onto a pillar-imbibed film over a narrow transition zone, with an apparent contact angle $\theta_{app} \sim 11°$. Sloped liquid surfaces refract light from the episcopic illumination, appearing darker in the top view image. Close to the droplet, the film surface appears evenly bright, indicating a flat

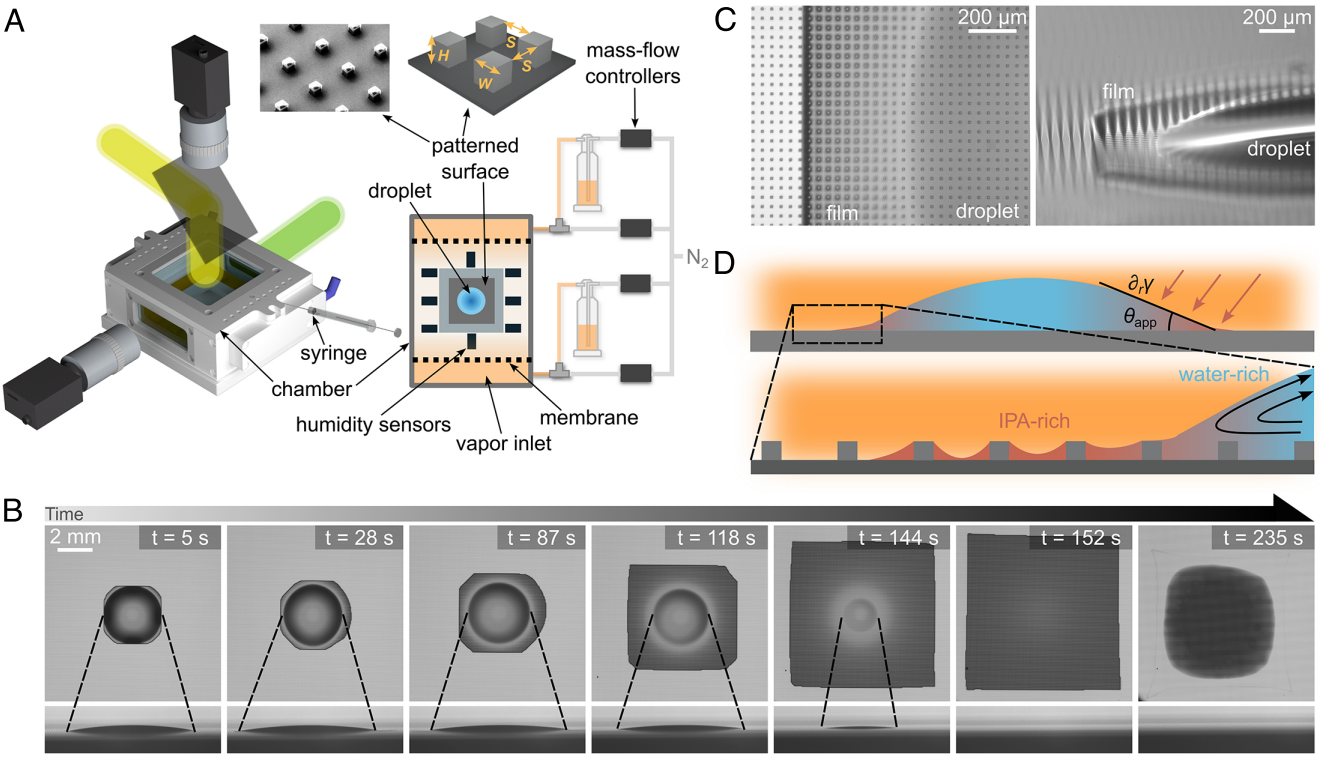


**Fig. 1.** Vapor-mediated wetting control on micropatterned surfaces. (*A*) Schematic of the experimental setup and SEM image of a micropillar decorated silicon wafer ($S = 30$ µm, $W = H = 10$ µm). (*B*) Wicking of water into hydrophilic textures is delayed more than 100-fold in an isopropyl alcohol (IPA) vapor atmosphere (images from top and side aspects, time $t$ since drop deposition). A Marangoni-contracted droplet coexists with a wicking film around it which effectively cloaks the pattern for the droplet. (*C*) High magnification photographs of the edge region of the drop-on-film configuration. (*D*) Schematic of the liquid configuration: a macroscopic droplet, connected to an imbibed film that thins and enriches in IPA away from the droplet.

film, level to the pillar tops. Approaching the outer boundary of the film, pillars increasingly pinch on the thinning film, leading to dark halos around them. The film terminates in a steep (dark) meniscus just before the first dry row of pillars. Over time, the film expands in a zipping-like motion (10) (*SI Appendix*, Extended Data Fig. S6): Once the terminal meniscus touches a pillar of the next row, capillary forces "pull along" the film to adjacent pillars. The droplet, in contrast, does not pin to the pillars but assumes a circular footprint and remains highly mobile, reminiscent of Marangoni-contracted droplets on flat surfaces (16, 17, 23–26).

**1.3. Interplay of Wicking and Contraction.** Next, we quantify the competition between capillary wicking and Marangoni contraction for the water/IPA system by varying pillar spacing, vapor concentration (characterized by the liquid IPA mass fraction in the bubbler, $\tilde{c}$), and droplet composition: Narrower pillar spacings $S$ are expected to generate a stronger wicking force (capillary pressure $p \sim S^{-1}$), while adding liquid IPA to the droplet or reducing the partial pressure of IPA in the atmosphere would reduce the rate of condensation and thus attenuate the Marangoni force. We start by varying $S$, keeping $\tilde{c} = 1$ and pure water as initial drop composition. The droplet and film dynamics can readily be quantified by the evolution of their footprint areas. Additionally, the apparent contact angle of the droplet indicates the strength of the contracting Marangoni force. We plot these quantities in Fig. 2*A* as a function of time. For $S = 30\,\mu$m (the case shown in Fig. 1), the plot indicates coexistence of drop and wicking film for about ~150 s, during which the apparent contact angle slowly decreases while the film and droplet areas remain approximately constant. This stage of delayed wicking and drop/film coexistence is significantly diminished when decreasing the pillar spacing to $S = 10\,\mu$m (*SI Appendix*, Extended Data Fig. S1*A* and Movie S2), yet still about an order of magnitude larger than the pure case (*SI Appendix*, Extended Data Fig. S1). When increasing the pillar spacing to $S = 50\,\mu$m (*SI Appendix*, Extended Data Fig. S1*B* and Movie S2), wicking is not only delayed, but completely inhibited for ~128 s. During this stage, the droplet is pinned to columns, rows, or diagonals of pillars, giving it an octagonal footprint shape.

High-resolution imaging of the contact line zone reveals the mechanism (*SI Appendix*, Extended Data Fig. S8 and Movie S8): The apparent contact angle of the contracted droplet remains larger than the aspect ratio of the gap between pillars, $\tan\theta_{app} > H/S$. Because the free surface is pinned to the last wetted row of pillars, the liquid now cannot reach the next row and the wicking force cannot develop, analogous to static wetting (10). This geometric threshold is different from the energetically motivated transition from partial wetting to hemiwicking (6, 7) because the apparent angle is determined by nonequilibrium processes while the microscopic angle is always below the critical angle for hemiwicking (17). Note also that the apparent angle remains much below the critical angle of hemiwicking (6,7), so it cannot be treated akin to a nonequilibrium Gibbs criterion (27). As IPA continues being absorbed into the droplet, contraction weakens until the wicking condition is reached (10). About 10 s later, a circular, Marangoni-contracted droplet emerges on top of an imbibed film, impassive of the substrate pattern and free to move.

Toward the end of the coexistence phase (Figs. 1*A* and 2*B*, $t \gtrsim 118$ s), the wicking film grows, drawing volume from the droplet. Quite remarkably, the growth rate of the film area $A$ always follows a standard hemiwicking power-law $A_{max} - A \sim t_f - t$, as was previously described for simple liquids and textures of various aspect ratios (8, 9, 21, 28–30). However, the flow in

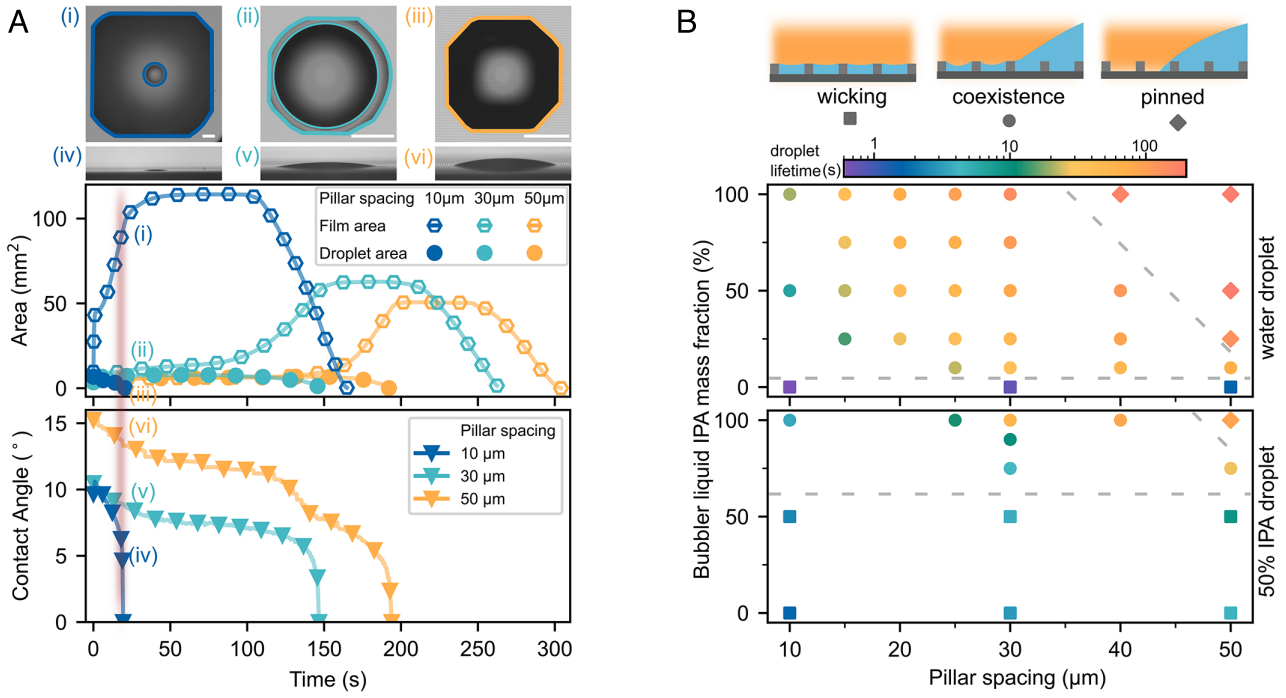


**Fig. 2.** Drop-film coexistence with varying texture spacing, vapor, and droplet concentrations for water/IPA. (*A*), *Top*: Evolution of the droplet footprint area (closed markers) and the total area liquid-covered area (film, open symbols). *Bottom*: apparent contact angle $\theta_{app}$ of the drop on surfaces with varying pillar spacing $S$ in IPA vapor environment. Images show top and side aspects at $t = 18$ s (Scale bars indicate 1 mm.) Smaller pillar spacings enhance the wicking force, leading to shorter drop and film lifetimes and smaller apparent contact angles of the drop. For $S = 50\,\mu$m, wicking is completely prevented initially [images (*iii*) and (*vi*)]. (*B*) Phase diagram of wetting behaviors vs. pillar spacing and IPA vapor concentration for water droplets (*Top*) and 50% IPA aqueous droplets (*Bottom*). Color indicates the lifetime of the contracted droplet (cf. *SI Appendix*, Extended Data Fig. S7). The IPA vapor concentration is characterized by the mass fraction of liquid IPA in the bubbler, $\tilde{c}$, indicative of the mismatch of drop-vapor equilibrium (*SI Appendix*).

our case is strongly impacted by Marangoni flows: The prefactor is decreased by about an order of magnitude as compared to the case without Marangoni flows (*SI Appendix*, Extended Data Fig. S9). In addition, wicking is initially fully suppressed, which cannot be captured by the classical law of hemiwicking. Once the droplet merged into the imbibed film, expansion ceases and the final evaporation regime begins (Fig. 1*B*, $t \gtrsim 152$ s). In this stage, the film breaks up into small menisci surrounding the pillars which subsequently dry from the periphery to the center of the film (*SI Appendix*, Extended Data Fig. S10 and Movie S9).

In Fig. 2*B*, we provide a phase diagram that summarizes these three distinct behaviors (immediate wicking □, coexistence ○, pinning ◊) as a function of $S$ and $\tilde{c}$, for initially pure water droplets (*Top*) and droplets with 50 wt% IPA (*Bottom*). The lifetime of the contracted droplet is indicated as color code. Generally, droplet lifetime increases with $S$ and $\tilde{c}$ because wicking forces decrease with pillar spacing while Marangoni forces are sustained longer in higher IPA vapor concentrations (see *SI Appendix*, Extended Data Figs. S1–S16 for plots of the footprint areas over time (*SI Appendix*, Fig. S11), drop lifetimes over $S$ (*SI Appendix*, Fig. S7), apparent contact angles and drop lifetimes for different drop compositions on flat and textured surfaces (*SI Appendix*, Fig. S12), and experiments with other liquid and vapor materials (*SI Appendix*, Fig. S4)). Already small amounts of IPA vapor delay the wicking process noticeably, especially for large pillar spacings, so that "immediate wicking" is limited to pure cases. Taking into account the nonideal evaporation condensation behavior of IPA and water, and integrating the rate of change of the droplet composition to estimate the lifetime of the Marangoni flows, droplet and film lifetimes can semiquantitatively be predicted (*SI Appendix*, *Mixture Droplet Evaporation-Condensation Dynamics* and Extended Data Figs. S13–S16). Since the pinned state emerges when the apparent contact angle from Marangoni contraction exceeds the pattern aspect ratio, that regime depends on vapor composition, pattern spacing, and pillar height $H$ (see *SI Appendix*, Extended Data Fig. S2 for experiments with varying $H$). Isotropic rescalings of the texture, in contrast, do not alter this transition, as confirmed in experiments with pillars of edge length $W = 5$ μm (*SI Appendix*, Extended Data Fig. S3). Still, increased viscous dissipation slows down transport through smaller patterns, extending the lifetime of the coexistence state.

## 2. Discussion

The existence of contracted droplets on top of an imbibed film allows for unprecedented liquid manipulation strategies on textured surfaces. A collection of possible manipulation sequences is shown in Fig. 3. We start by showing that fully imbibed liquids can reversibly be extracted into contracted droplets (Fig. 3*A* and Movie S3): A water droplet, deposited in a moist atmosphere, fully wicks into the texture immediately. By use of the gas mixing system, we then switch the vapor in the atmosphere from water to IPA. This causes an instability of the film which develops into a Marangoni-contracted droplet ($\theta_{app} \sim 9°$). The droplet is still surrounded by an extended film that is, on average, much thinner than the pillar height, rendered dark by capillary rise on the pillar side walls. Returning to pure water vapor in the atmosphere, the droplet is imbibed back into the surface texture, and the extraction process can be repeated by switching between vapor types. In *SI Appendix*, Extended Data Fig. S4 we show the same process, but using ethylene glycol (EG) droplets or ethanol vapor, demonstrating its generality.

Different film shapes (e.g. square, hexagon, elongated hexagon, irregular) emerge from the interplay of pillar shapes and lattice symmetries, as shown in Fig. 3*B* and Movie S4, caused by anisotropic spreading resistances, analogous to the shape formation on wicking (10, 31, 32) or nonwicking patterned surfaces (33–35). The pillar shape modulates the film wicking, as highlighted in panels (*ii*) and (*iii*): The lattice is identical in both cases, but the pronounced edges of the triangular pillars in (*iii*) increase pinning forces in some directions, breaking the equilateral symmetry of the final hexagonal film shape.

For strong lattice anisotropies, wicking and pinning states may coexist along different axes (Fig. 3 *B*, *iv*), leading also to highly anisotropic droplet mobility. In the case shown in Fig. 3 *B*, *iv*, $S_x = 70$ μm and $S_y = 10$ μm effectively provide rails keeping the droplet mobile only in $y$-direction. The drop/film coexistence effect pertains to random arrangements (panel *v*), where a circular, contracted droplet is surrounded by an irregular film, demonstrating that our strategy may be applicable to a wide variety of surface patterns that need not be specifically designed for the dewetting process.

Based on the observation that smaller pillar spacings give rise to stronger wicking forces, surfaces can also readily be designed to induce droplet motion and thus directional wetting/drying: Fig. 3*C* (Movie S5) shows a contracted droplet (pure water in IPA vapor) on a lattice with a unidirectional spacing gradient, $S_y = 35$ μm to 15 μm, while $S_x = 30$ μm. After depositing the droplet, the liquid wicks faster in the direction of decreasing pillar spacing. Because droplet motion and film spreading are coupled, the entire liquid body moves down the pillar spacing gradient.

The sensitivity to vapor composition also allows for contactless droplet manipulation on micropatterned substrates, which is demonstrated in Fig. 3*D* (Movie S6). There, IPA vapor was injected on the left, water vapor on the right end of the environmental chamber, generating a constant and homogeneous vapor composition gradient. In this environment, the water droplet moves toward the water vapor side, caused by faster IPA absorption and thus stronger Marangoni forces on the opposite side, analogous to the case on flat surfaces (16). Utilizing both, preferential spreading and vapor gradient actuation, droplets can be guided along complex paths, as shown in (Fig. 3 *E* and Movie S6. Here, a pillar pattern ($S = 30$ μm) bounded by an S-shaped outline guides the liquid, and a vapor gradient analogous to panel (*D*) induces the motion.

The examples from Fig. 3 demonstrate the versatility of manipulating droplets on textured surfaces dynamically through vapors in the environment. The effect is easily implemented, highly reproducible, and robust against variations of pattern properties and vapor compositions (Fig. 2). It also generalizes to arbitrary combinations of liquids, requiring only miscibility and a lower surface tension of the excess vapor component (see *SI Appendix*, Extended Data Fig. S4 for water–ethanol and EG–IPA pairs). While wicking can temporarily also be suppressed by the evaporative contact angle in highly volatile liquids, the vapor-induced Marangoni fluxes may last orders of magnitude longer and are tunable to extract rather than evaporate previously imbibed liquids from the texture. In contrast to lubricant infused surfaces (36), here the liquid components are volatile and miscible, thus eliminating the need for separate infusion and removal of lubricant, akin to self-lubricating droplets (37). Notably, the wicking force per unit length of contact line is governed only by ratios of the geometric parameters $S$, $W$, and $H$, but remains independent of the absolute length scale (7), ensuring broad applicability across a wide range of scales

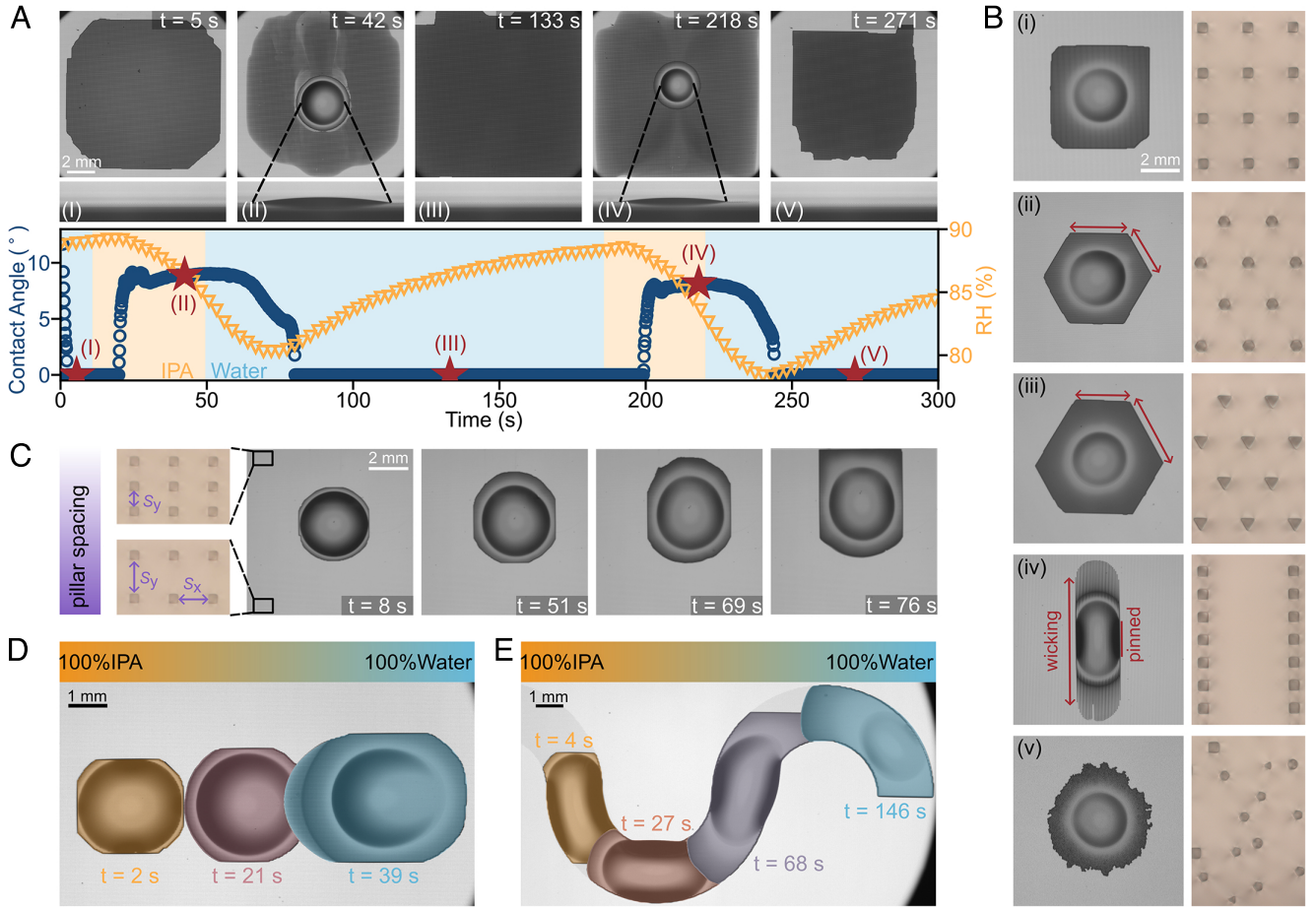


**Fig. 3.** Vapor-mediated droplet manipulation on patterned surfaces. (*A*) Repeatable liquid extraction from fully imbibed films by switching between water and IPA vapor in the atmosphere. We plot the apparent contact angle of the droplet, $\theta_{app}$ (blue), and the relative humidity in the chamber, *RH* (yellow), vs. time *t* since deposition (red stars indicate picture times, background color indicates mass flow controller setting. $S = 30\,\mu m$, $W = H = 10\,\mu m$). (*B*) Impact of lattice symmetry and pillar shape, for similar pillar area fraction $\phi_p \sim 0.065 \pm 0.003$ (pure water drop in IPA vapor): (*i*) square pillars on a square lattice, (*ii*) hexagonal pillars on a hexagonal lattice, (*iii*) triangular pillars on a hexagonal lattice, (*iv*) square pillars on a rectangular lattice, and (*v*) random shapes in random arrangement. Wicking forces are governed by the lattice, but pinning is modified by pillar shape. (*C*) Directional film spreading and drop motion on a square lattice with spacing gradient ($S_y = 35\,\mu m to 15\,\mu m$, $S_x = 30\,\mu m$, pure water drop in IPA vapor). (*D*) Droplet motion on a homogeneous square lattice ($S = 30\,\mu m$) with IPA vapor gradient. (*E*) Droplet forced along a square pillar lattice within "S"-shaped bounds ($S = 30\,\mu m$) by a vapor gradient in *x*-direction.

(*SI Appendix*, Extended Data Fig. S3). Still, viscous dissipation and thus the rate of wicking depends on the scale of the texture, expanding the duration of the coexistence regime for smaller structures (*SI Appendix*, Extended Data Fig. S2 and *Wicking Dynamics*). This inherent scalability thus leaves a significant degree of freedom for the design of surface patterns or choice of chemicals, facilitating its application in the processing of surface microstructures, liquid collection and extraction techniques, or sensing device applications.

## 3. Materials and Methods

**3.1. Preparation of Surface Patterns.** The micropillar arrays were fabricated by direct laser writing lithography of a negative photoresist. First, the silicon wafers (CZ-Si, (100), 500(50) µm, p-type, MicroChemicals GmbH) were cleaved into square pieces of 25 mm × 25 mm. The cleaved substrates were then sequentially rinsed with deionized water, acetone, and isopropanol, followed by drying with nitrogen gas and baking at 150 °C to remove moisture thoroughly. Next, the photoresist [SU-8 3025 (for 20 µm high pillars), 3010 (for 10 µm high pillars) & 3005 (for 5 µm high pillars), KAYAKU Advanced Materials] was spin-coated onto the substrate. Subsequently, the wafer was soft-baked at 95 °C for 5 min (3005 & 3010) or 15 min (3025). Then, the wafer was exposed in the direct laser writer (POLOS NanoWriter Advanced, PM-100). Thereafter, a postexposure baking was conducted at 95 °C for 3 min (3005 & 3010) or 5 min (3025). Finally, the patterned substrate was rinsed thoroughly in SU-8 developer and dry-blown with nitrogen.

**3.2. Experimental Setup.** The experimental setup consisted of a custom-designed environmental chamber (Internal dimensions $L = 85$ mm × $W = 75$ mm × $H = 33$ mm), a vapor generation system, and an imaging system that recorded top and side aspects of the droplets through windows in the chamber. The chamber was well sealed against the ambient to ensure stable vapor environments inside. The left and right walls of the main chamber were composed of cloth membranes, behind which two separate spout chambers were located. These spout chambers were flushed with a continuous stream of nitrogen containing the vapors. This way, vapors were only diffusively injected into the main chamber, generating a stable, quiescent atmosphere. Eight humidity sensors (Honeywell HIH-4000) were integrated into the main chamber to measure the humidity distribution.

The vapors were prepared by a custom-built gas mixing system, consisting of two identical lines, one for each side of the chamber. Each line consisted of two mass flow controllers (MKS Instruments, MF1, 500 sccm), where the output flux of one controller was bubbled through a gas wash bottle, containing mixtures of the same components as the droplet at the desired vapor composition. We used ultrapure water (Milli-Q, resistivity 18.2 MΩ cm), isopropanol (VWR, 99.7+%), ethylene glycol (Carl Roth, 99.5+%), and ethanol (VWR, absolute) as liquids for droplets and in the gas wash bottles. Vapor compositions are quantified

by the mass fraction of the liquids in the bubblers (see *SI Appendix*, Extended Data Fig. S13 for the relation to actual vapor partial pressures for water/IPA mixtures). The gas wash bottles were placed into a thermal bath ($T = 22\,°C$) to compensate for evaporative cooling. The two fluxes were then unified and injected into the spout chamber. The total mass flux (i.e., the sum of the two fluxes) was kept constant across all experiments, only the ratio of the two fluxes was varied. Experiments with static, homogeneous atmosphere were performed with 100% of the flux passing through the gas wash bottle. Note that the vapor always remained undersaturated to prevent condensation on solid surfaces (*SI Appendix*, Extended Data Fig. S13) and keep the drying times of the films finite. Liquids in the bottles were replaced after each experiment to ensure constant composition of the liquids in the bubblers. The vapor composition gradient was created by filling pure isopropanol and pure water to the gas wash bottles for the two sides. For the extraction experiments where we switched between different vapors, gas lines were reconfigured to simultaneously switch vapors on both sides.

The imaging system consisted of two collimated illuminators and two cameras. For the top view perspective, the light of a custom-designed Köhler-type illuminator was projected by a 50/50 beamsplitter onto the sample, reflected by the substrate, and recorded by a macrolens (Schneider optics 50 mm) and a monochromatic CMOS camera (FLIR Grasshopper). High magnification images were taken with a zoom lens (Thorlabs MVL12X3Z). The side aspect was recorded with a telecentric lens (Thorlabs 1.0X Bi-Telecentric lens) and an identical CMOS camera. Illumination was provided from the rear with a telecentric illuminator (Edmund optics, 52 mm). Image analysis was done by a self-developed Python script.

**3.3. Experimental Procedure.** Before each experiment, the substrate was cleaned with deionized water and isopropanol, then dried using nitrogen gas. Then, the substrate was plasma treated in a plasma oven (13.56 MHz, Diener electronic GmbH) for one minute and immediately transferred into the chamber. After the vapor environment in the chamber stabilized according to the readings from the humidity sensors, liquid droplets with volumes from 0.5 µl to 1 µl were deposited onto the substrate with a clean precision syringe (Hamilton Gas-tight Series 1700, 10 µl). The delay between plasma treatment and droplet deposition was always less than 3 min. To minimize exchange between the atmosphere in the chamber and the liquid in the syringe prior to depositing the droplet, air was drawn into the needle before inserting it into the chamber through a small hole next to the top window.

**Data, Materials, and Software Availability.** All study data are included in the article and/or supporting information. The raw imagery, the analysis and modeling code and associated processed data have been deposited in OSF: https://doi.org/10.17605/OSF.IO/8NJ6X (38).

**ACKNOWLEDGMENTS.** We thank Nate Cira, Adrien Benusiglio, Manu Prakash, and Hans Riegler for discussions. We are indebted to Louis Kukk, Kris Handtke, and Wolf Keiderling for assistance with the technical realization of the setup. We acknowledge the use of the experimental equipment and the expert support concerning its usage and data analysis provided by the Nanostructure Laboratory at the University of Konstanz. R.S. was supported by the German Research Foundation (DFG, grant no. 422877263). Z.X. was supported by China Scholarship Council (CSC202206090036).

Author affiliations: [a]Department of Physics, University of Konstanz, Konstanz 78457, Germany; and [b]Departamento de Materiales de Baja Dimensionalidad, Instituto de Investigaciones en Materiales, Universidad Nacional Autónoma de Mexico (IIM-UNAM), Ciudad Universitaria, Coyoacán, 04510, Ciudad de México, Mexico

1. D. Lohse, X. Zhang, Physicochemical hydrodynamics of droplets out of equilibrium. *Nat. Rev. Phys.* **2**, 426–443 (2020).
2. D. Bonn, J. Eggers, J. Indekeu, J. Meunier, E. Rolley, Wetting and spreading. *Rev. Mod. Phys.* **81**, 739–805 (2009).
3. P. G. de Gennes, F. Brochard-Wyart, D. Quéré, *Capillarity and Wetting Phenomena: Drops, Bubbles, Pearls, Waves* (Springer, 2004).
4. S. Howison, J. Moriarty, J. Ockendon, E. Terrill, S. Wilson, A mathematical model for drying paint layers. *J. Eng. Math.* **32**, 377–394 (1997).
5. T. Tanaka, M. M. M. Morigami, N. A. N. Atoda, Mechanism of resist pattern collapse during development process. *Jpn. J. Appl. Phys.* **32**, 6059 (1993).
6. D. Quéré, Wetting and roughness. *Annu. Rev. Mater. Res.* **38**, 71–99 (2008).
7. J. Bico, U. Thiele, D. Quéré, Wetting of textured surfaces. *Colloids Surf. A Physicochem. Eng. Asp.* **206**, 41–46 (2002).
8. J. Kim, M. W. Moon, H. Y. Kim, Dynamics of hemiwicking. *J. Fluid Mech.* **800**, 57–71 (2016).
9. B. Natarajan *et al*., Predicting hemiwicking dynamics on textured substrates. *Langmuir* **37**, 188–195 (2020).
10. L. Courbin *et al*., Imbibition by polygonal spreading on microdecorated surfaces. *Nat. Mater.* **6**, 661–664 (2007).
11. K. H. Chu, R. Xiao, E. N. Wang, Uni-directional liquid spreading on asymmetric nanostructured surfaces. *Nat. Mater.* **9**, 413–417 (2010).
12. C. Liu *et al*., Long-range spontaneous droplet self-propulsion on wettability gradient surfaces. *Sci. Rep.* **7**, 7552 (2017).
13. L. Yang *et al*., Selective directional liquid transport on shoot surfaces of crassula muscosa. *Science* **384**, 1344–1349 (2024).
14. J. Li *et al*., Topological liquid diode. *Sci. Adv.* **3**, eaao3530 (2017).
15. L. Mekhitarian, B. Sobac, S. Dehaeck, B. Haut, P. Colinet, Evaporation dynamics of completely wetting drops on geometrically textured surfaces. *Europhys. Lett.* **120**, 16001 (2017).
16. N. J. Cira, A. Benusiglio, M. Prakash, Vapour-mediated sensing and motility in two-component droplets. *Nature* **519**, 446–450 (2015).
17. S. Karpitschka, F. Liebig, H. Riegler, Marangoni contraction of evaporating sessile droplets of binary mixtures. *Langmuir* **33**, 4682–4687 (2017).
18. D. A. Baumgartner, S. Shiri, S. Sinha, S. Karpitschka, N. J. Cira, Marangoni spreading and contracting three-component droplets on completely wetting surfaces. *Proc. Natl. Acad. Sci. U.S.A.* **119**, e2120432119 (2022).
19. L. Yang, A. A. Pahlavan, H. A. Stone, C. D. Bain, Evaporation of alcohol droplets on surfaces in moist air. *Proc. Natl. Acad. Sci. U.S.A.* **120**, e2302653120 (2023).
20. A. A. Pahlavan, L. Yang, C. D. Bain, H. A. Stone, Evaporation of binary-mixture liquid droplets: The formation of picoliter pancakelike shapes. *Phys. Rev. Lett.* **127**, 024501 (2021).
21. C. Ishino, M. Reyssat, E. Reyssat, K. Okumura, D. Quere, Wicking within forests of micropillars. *Europhys. Lett.* **79**, 56005 (2007).
22. T. Gambaryan-Roisman, Liquids on porous layers: Wetting, imbibition and transport processes. *Curr. Opin. Colloid Interface Sci.* **19**, 320–335 (2014).
23. Y. Tsoumpas, S. Dehaeck, A. Rednikov, P. Colinet, Effect of marangoni flows on the shape of thin sessile droplets evaporating into air. *Langmuir* **31**, 13334–13340 (2015).
24. A. Benusiglio, N. J. Cira, M. Prakash, Two-component marangoni-contracted droplets: Friction and shape. *Soft Matter* **14**, 7724–7730 (2018).
25. O. Ramírez-Soto, S. Karpitschka, Taylor dispersion in thin liquid films of volatile mixtures: A quantitative model for marangoni contraction. *Phys. Rev. Fluids* **7**, l022001 (2022).
26. J. Charlier, A. Rednikov, S. Dehaeck, P. Colinet, D. Terwagne, Water-propylene glycol sessile droplet shapes and migration: Marangoni mixing and separation of scales. *J. Fluid Mech.* **933**, A45 (2022).
27. Y. Tsoumpas *et al*., Nonequilibrium Gibbs' criterion for completely wetting volatile liquids. *Langmuir* **30**, 11847–11852 (2014).
28. N. Srivastava, C. Din, A. Judson, N. C. MacDonald, C. D. Meinhart, A unified scaling model for flow through a lattice of microfabricated posts. *Lab Chip* **10**, 1148–1152 (2010).
29. J. Kim, M. W. Moon, K. R. Lee, L. Mahadevan, H. Y. Kim, Hydrodynamics of writing with ink. *Phys. Rev. Lett.* **107**, 264501 (2011).
30. S. R. Krishnan, J. Bal, S. A. Putnam, A simple analytic model for predicting the wicking velocity in micropillar arrays. *Sci. Rep.* **9**, 20074 (2019).
31. L. Courbin, J. C. Bird, M. Reyssat, H. A. Stone, Dynamics of wetting: from inertial spreading to viscous imbibition. *J. Phys. Condens. Matter* **21**, 464127 (2009).
32. H. Sontheimer, A. T. Ho, L. Elsäßer, P. Stephan, T. Gambaryan-Roisman, "Numerical simulation of drop impingement onto superheated textured walls" in *Journal of Physics: Conference Series*, B. Šarler, L. Vanoli, T. Dobravec, Eds. (IOP Publishing, 2024), vol. 2766, p. 012085.
33. J. Lou *et al*., Polygonal non-wetting droplets on microtextured surfaces. *Nat. Commun.* **13**, 2685 (2022).
34. R. Raj, S. Adera, R. Enright, E. N. Wang, High-resolution liquid patterns via three-dimensional droplet shape control. *Nat. Commun.* **5**, 4975 (2014).
35. K. M. Al Balushi, G. Duursma, P. Valluri, K. Sefiane, D. Orejon, Binary mixture droplet evaporation on microstructured decorated surfaces and the mixed stick-slip modes. *Langmuir* **39**, 8323–8338 (2023).
36. T. S. Wong *et al*., Bioinspired self-repairing slippery surfaces with pressure-stable omniphobicity. *Nature* **477**, 443–447 (2011).
37. H. Tan, D. Lohse, X. Zhang, Self-lubricating drops. *Curr. Opin. Colloid Interface Sci.* **68**, 101744 (2023).
38. R. Saiseau, Z. Xu, S. Karpitschka, Vapor-mediated wetting and imbibition control on micropatterned surfaces. Open Science Framework. https://doi.org/10.17605/OSF.IO/8NJ6X. Deposited 18 December 2025.